https://doi.org/10.5194/egusphere-2026-2934
Preprint. Discussion started: 19 June 2026

Sensitivity of convective cloud and rainfall responses to urban aerosol emission strengths

Friederike Keil[1], Markus Quante[1], Bernd Heinold[2], and Volker Matthias[1]

[1]Helmholtz-Zentrum Hereon, Geesthacht, Germany
[2]Leibniz Institute for Tropospheric Research, Leipzig, Germany

Correspondence: Friederike Keil (friederike.keil@hereon.de)

Abstract. Urban aerosol emissions can modify convective precipitation through aerosol-cloud interactions, yet the sensitivity of convective events to emission strength and its detectability against meteorological variability remain poorly constrained. We investigate aerosol-cloud-precipitation interactions using the COSMO-DCEP-MUSCAT model system with direct aerosol-cloud coupling, systematically varying urban emission strengths across a wide scaling range for two differing mid-latitude convective cases. Lagrangian trajectory analysis tracks air volume transport from urban sources into convective regions, complemented by ensemble simulations to separate emission-induced changes from natural meteorological variability.

Results reveal a strong dependence on meteorological conditions. Under moderate convective instability, high emission scaling factors trigger ice-phase invigoration through enhanced ice nucleation and latent heat feedback, producing substantial increases in ice content and precipitation intensity accompanied by spatial expansion and temporal shifts. Emission-response analysis reveals nonlinear behavior, with low-to-moderate scaling factors producing no systematic response while high scaling factors trigger substantial microphysical modifications. Under stronger convective instability, even the highest emission scaling factors produce only modest microphysical responses and spatial redistribution rather than intensification, as strong background dynamics buffer aerosol-induced impacts. Ensemble analysis demonstrates that robust signals emerge only for selected variables during specific convective stages, with most responses remaining comparable to natural atmospheric variability.

These results indicate that detectable precipitation responses require strong emission perturbations under favorable meteorological conditions, with effects manifesting as intensity changes and spatial and temporal redistribution. The convective regime critically determines the magnitude and detectability of aerosol effects, with implications for understanding urban impacts on precipitation across different atmospheric environments.

1 Introduction

As cities continue to grow and emission regulations evolve, understanding the response of convective precipitation to locally emitted aerosol perturbations becomes increasingly important for urban planning and climate adaptation strategies. While previous studies have established that urban aerosol emissions can modify convective precipitation patterns through changes in cloud microphysics (Van Den Heever and Cotton, 2007; Han et al., 2012; Sarangi et al., 2018), the quantitative relationship

https://doi.org/10.5194/egusphere-2026-2934
Preprint. Discussion started: 19 June 2026

between emission strength and precipitation response has received limited systematic investigation, particularly for convective events over mid-latitude urban areas. Uncertainties arise from the complexity of aerosol-cloud-precipitation interactions. Depending on their physicochemical properties, urban aerosol particles can act as cloud condensation nuclei (CCN), modifying the droplet size distribution of warm clouds, or as ice-nucleating particles (INP), influencing ice formation in mixed-phase and cold clouds (Pruppacher and Klett, 1997).

The increased CCN concentrations simultaneously affect multiple competing processes: they can delay warm-rain formation while enhancing latent heat release (Cotton and Walko, 2021), suppress coalescence while invigorating updrafts (Fan et al., 2025), and modify ice-phase processes in ways that either enhance or suppress precipitation (Rosenfeld et al., 2008). The net effect depends on which mechanisms dominate under given meteorological conditions. Distinguishing actual aerosol effects from model noise and identifying potential threshold behaviors therefore requires systematic investigation across a range of emission scenarios, combined with a understanding of how aerosol perturbations propagate through the cloud system via microphysical modifications and dynamical feedback.

Several observational and modeling studies have examined urban effects on convective precipitation, though results remain inconsistent among the studies. Fagunloye and Diem (2025) found evidence for precipitation enhancement downwind of urban areas, attributing the signal to thermodynamic and aerosol effects and suppression under different synoptic conditions. Modeling studies have similarly highlighted the regime dependence of these interactions (Zhong et al., 2017; Barthlott and Hoose, 2018), with aerosol effects on precipitation magnitude and spatial distribution varying substantially between cases characterized by weak and strong synoptic forcing. Many of these studies compare only two discrete aerosol scenarios, typically representing clean and polluted conditions, without exploring intermediate loading levels or a broader range of emission strengths (Xiao et al., 2016; Zheng et al., 2020; Souri et al., 2020). While such binary comparisons provide useful qualitative insights into the direction of aerosol effects, they cannot resolve the quantitative relationship between aerosol loading and precipitation response, nor determine whether these effects scale systematically with emission strength. Studies that do vary aerosol loading more systematically often prescribe spatially uniform CCN concentrations across discrete clean-to-polluted categories (Barthlott and Hoose, 2018; Lucas et al., 2025) rather than modifying the underlying emission fields, and therefore do not capture the spatially heterogeneous aerosol fields characteristic of urban aerosol plumes nor the full aerosol life cycle from emission through transport and transformation to cloud interaction. Systematic investigations that vary emission strength across a wide scaling range within a fully coupled aerosol-transport-microphysics framework therefore remain scarce, particularly for mid-latitude European urban environments.

Keil et al. (2025) recently carried out a regional interactive aerosol-cloud modelling study at convection-resolving scale, investigating the influence of modest urban emission perturbations on cloud microphysics and precipitation for two differing meteorological cases. Their results show that the resulting modifications are modest but statistically significant in certain parts of the cloud fields and highly case-dependent, making general assertions about urban impacts challenging. However, their focus on small, modest emission perturbations leaves the question open of how these interactions scale across a broader range of emission strengths and whether the observed effects follow a systematic relationship with emission magnitude.

https://doi.org/10.5194/egusphere-2026-2934
Preprint. Discussion started: 19 June 2026

Building on these findings, we investigate the sensitivity of precipitating convective events to systematic variations in urban emission strength, ranging from values representative of current emissions of Leipzig, one of the fastest-growing major cities in Germany, to scalings several orders of magnitude beyond, to characterize how aerosol effects on convective precipitation scale with emission strength and to identify where systematic responses emerge above the background of meteorological variability. We examine two convective cases that interact with the urban aerosol plume of Leipzig, providing well-constrained conditions for studying urban emission impacts under differing meteorological conditions. Using the online-coupled model system COSMO-DCEP-MUSCAT (Wolke et al., 2004, 2012; Heinold et al., 2019) with an integrated urban parameterization and a two-moment bulk microphysics scheme that incorporates MUSCAT-simulated aerosol fields into the activation of cloud droplets and ice crystals, we systematically scale emission strengths and track polluted air volumes from their sources into convective regions to quantify how cloud microphysical properties, dynamics, and precipitation respond to varying levels of urban aerosol loading.

The paper is structured as follows. Section 2 describes the model system, the two convective cases, and the experimental design. Section 3 presents the results, including microphysical and dynamical responses to varying emission strengths, a emission-response analysis across all scaling experiments, and an ensemble-based robustness assessment. Section 4 provides a discussion of the results, addresses limitations of the modeling approach, and draws conclusions from both the emission-response and ensemble analyses.

2 Methods

2.1 Model

Our simulations employ COSMO (COnsortium for Small scale MOdelling) version 5.05, a non-hydrostatic regional numerical weather prediction model (Schättler et al., 2018), which is online-coupled with the chemistry transport model MUSCAT (MUltiScale Chemistry Aerosol Transport) (Wolke et al., 2004, 2012). Within this coupled framework, MUSCAT is driven by the meteorological fields from COSMO and solves a system of three-dimensional, time-dependent advection–diffusion–reaction equations to simulate the transport and chemical transformation of both gas-phase species and aerosol populations. The aerosol representation follows a hybrid bulk–bin approach, which constitutes the standard configuration for air quality applications (Wolke et al., 2012). This approach encompasses 25 prognostic particle tracers: primary PM2.5 and PM10, primary organic carbon (POC), elemental carbon (EC), sulfate, nitrate, ammonium, secondary organic aerosol (SOA), six size-resolved classes for sea-salt and marine organics (0.01 - 10 μm), and five size-resolved classes for desert dust (0.2 - 48 μm). An external mixture assumption is applied to all aerosol species. Online parameterizations describe natural aerosol sources such as desert dust and sea spray, while a biogenic emission scheme is also incorporated. The model explicitly accounts for secondary organic aerosol formation and multiphase chemistry, whereas anthropogenic emissions of primary particles and their precursors are specified using contemporary emission inventories. The representation of transport includes advection, turbulent diffusion, sedimentation, as well as dry and wet deposition processes. Meteorological fields required by MUSCAT, such as wind components,

https://doi.org/10.5194/egusphere-2026-2934
Preprint. Discussion started: 19 June 2026

vertical diffusivities, and boundary-layer resistances, are directly supplied by COSMO. The online coupling architecture enables bidirectional feedback, allowing simulated aerosol distributions to affect radiation and cloud processes within COSMO.

To account for the distinct microclimate characteristics of urban environments, we employ the double-canyon urban canopy parameterization (DCEP) (Schubert et al., 2012). DCEP extends the Building Effect Parameterization (BEP) of Martilli et al. (2002) by incorporating radiative interactions between two adjacent urban canyons. The parameterization represents urban canopy structures through three element categories: ground, walls, and roofs, which are arranged in idealized double-street-canyon segments. During a preprocessing stage, the horizontal distribution of these segments within each model grid cell is established, and both probabilistic and geometric properties of the canopy elements are derived from a high-resolution building geometry dataset available for Saxony. During model integration, DCEP computes surface fluxes of momentum, heat, and turbulent kinetic energy (TKE), while also resolving radiative transfer and thermal balance equations for each canopy component. This approach provides a physically consistent representation of heat transfer dynamics, radiative exchange, and airflow patterns within urban street canyons.

Cloud microphysics are represented using the two-moment bulk scheme of Seifert and Beheng (2006b, a), which predicts mass mixing ratios and number concentrations for six hydrometeor categories: cloud droplets, raindrops, cloud ice, snow, graupel, and hail. In contrast to the standard scheme, which relies on prescribed CCN and INP concentrations, droplet and ice particle activation are computed prognostically from MUSCAT-simulated aerosol mass concentrations, enabling a spatially and temporally variable representation of aerosol-cloud coupling. For cloud droplet activation, the parameterization of Abdul-Razzak and Ghan (2000) is applied, which derives the number of activated particles from the size distribution and hygroscopicity of multiple aerosol species, with the maximum supersaturation emerging from the balance between updraft-driven cooling and the competing uptake of water vapor by the aerosol population. Ice nucleation is treated following Weger et al. (2018), accounting for the contribution of dust, soot, and organic carbon to heterogeneous ice formation.

2.2 Simulation setup and experiments

Two convective precipitation events in the central-eastern German region near Leipzig (51.34°, N, 12.37°, E) with different meteorological characteristics, though both characterized by substantial rainfall, were selected. While case I features a small-scale convective event with northerly winds on 13 July 2019, case II shows a larger event with westerly inflow on 20 July 2019. The differing inflow directions result in distinct background aerosol compositions, with sulfate dominating in case I and secondary organic aerosols and ammonium sulfate prevailing in case II. These contrasting events allow a robust examination of urban aerosol effects under varying meteorological conditions. A comprehensive description of the model configuration and both convective cases is provided by Keil et al. (2025).

Both cases are simulated with a 3-step one-way nesting strategy, where the outer most domain covers Europe (D0) with 14 km resolution and 40 vertical layers up to 22 km altitude (Fig. 1). In this domain, COSMO-MUSCAT employs the single-moment microphysics scheme, a 15 day chemistry spin-up, and 48 hour meteorological re-initialization cycles. Simulations are driven by ERA5 reanalysis (Hersbach et al., 2020) and initialized with CAMS chemical composition data (Inness et al., 2019). Anthropogenic emissions come from CAMS-REG (Granier et al., 2019) with CAMS-REG-TEMPO temporal profiles

https://doi.org/10.5194/egusphere-2026-2934
Preprint. Discussion started: 19 June 2026

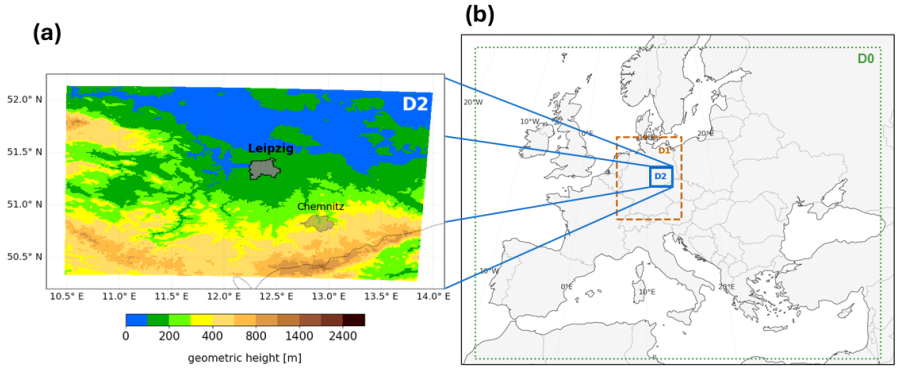

Figure 1. (a) Inner model domain D2 showing surface height. The cities Leipzig and Chemnitz are shown as filled areas in grey and light grey, respectively, to indicate their urban extent. (b) Model domains used in the simulation: D0 (14 km grid spacing), D1 (2.3 km), and D2 (1 km).

(Guevara et al., 2021). The inner domain D1 covers Germany at 2.3 km resolution with 50 vertical levels, using COSMO-D2 reanalysis from DWD as meteorological input. Each case runs for 48 hours (24 hour meteorological spin-up plus 24 hour coupled simulation) with two-moment microphysics. Emissions are based on the GRETA dataset (Schneider et al., 2016). The innermost domain D2 focuses on Leipzig at 1 km resolution, driven by D1 outputs. It employs the modified two-moment microphysics scheme, in combination with the urban parametrization DCEP activated for Leipzig. The output is saved at 10-minute intervals.

We conducted nine different experiments on the D2 domain. The first experiment (BASE) represents the reference simulation without any alterations. In the other experiments the emissions within the urban area of Leipzig were systematically varied (Tab. 1). We scaled the urban emissions by factors ranging from 0 to 5000, while keeping regional background emissions constant. This isolates the urban aerosol contribution and allows to quantify the precipitation sensitivity to urban emission strength across a wide range of magnitudes. All surface parameters and the urban parametrization remained unchanged for Leipzig.

For both the BASE and the URBANx500 experiments, a five-member ensemble was constructed by varying the length of the meteorological spin-up run, with spin-up lengths of 24, 21, 18, 15, and 12 h. The URBANx500 scaling was selected because it marks the onset of systematic microphysical responses in case I, as shown in the emission-response analysis (Section 3.2.1), and was applied consistently across both cases to allow direct comparison. To ensure consistent large-scale meteorological forcing, all ensemble members are driven by the same D1 simulation, allowing the impact of slightly varying initial meteorological conditions on the results to be assessed.

https://doi.org/10.5194/egusphere-2026-2934
Preprint. Discussion started: 19 June 2026

Table 1. Overview of numerical experiments with emission scaling factors relative to current Leipzig emissions and ensemble availability.

Experiment	Emission scaling	Ensemble
BASE	x 1	yes
NONURBAN	x 0	no
URBANx2	x 2	no
URBANx4	x 4	no
URBANx10	x 10	no
URBANx100	x 100	no
URBANx500	x 500	yes
URBANx1000	x 1000	no
URBANx5000	x 5000	no

2.3 Analysis method

2.3.1 Trajectory analysis

To trace air volumes influenced by urban emissions, we calculated backward trajectories using LAGRANTO (Sprenger and Wernli, 2015) from D2 meteorological fields (Fig. 2). Trajectories started from a region centered on the area of highest precipitation downwind of Leipzig and were traced back six hours for both cases. Backward trajectories for case I were initialized at 23:00 UTC on 13 July 2019, with a starting region covering approximately $40 \times 40\ \mathrm{km}^2$ horizontally (5 km starting point spacing) and $1 - 4.5\ \mathrm{km}$ vertically (20 levels). For case II, the initialization time was 22:00 UTC on 20 July 2019, using a starting region spanning roughly $40 \times 60\ \mathrm{km}^2$ at 5 km horizontal spacing between trajectory starting points and $1 - 7.5\ \mathrm{km}$ vertically (50 levels). Only backward trajectories passing below $1\ \mathrm{km}$ altitude over the urban area were retained, ensuring that analyzed air volumes had interacted with urban emissions prior to reaching the precipitation zone (Fig. 2).

For analyzing cloud dynamics and microphysics along the trajectories, a moving box analysis was implemented. At each time step, a rectangular box is centered on the mean urban trajectory point of each ensemble member, and vertical profiles are extracted by horizontally averaging all grid point values within the box, including grid points with zero values (unconditional average). Each box is defined in the COSMO rotated geographical coordinate system as a rectangular area with the trajectory point at its center, extending symmetrically in both horizontal directions (east–west and north–south) and including the full vertical column of model layers. The box is repositioned following the trajectory points in chronological order, tracking the analysis volume from the urban emission region toward the precipitation area. Box sizes were selected to match the spatial scale of each precipitation system. For case I, an approximately $15 \times 15\ \mathrm{km}^2$ box was chosen to enclose the smaller, localized precipitation structure (Fig. 2a), which contains a single convective cell dominating the precipitation field throughout the analyzed time period. For case II, a $35 \times 35\ \mathrm{km}^2$ box was used to capture the broader precipitation area (Fig. 3a), which may

https://doi.org/10.5194/egusphere-2026-2934
Preprint. Discussion started: 19 June 2026

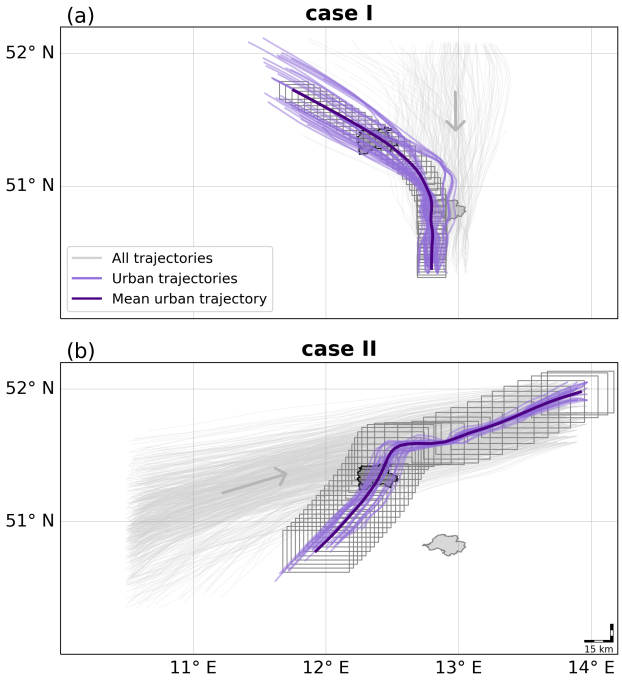

Figure 2. Trajectories for case I (a) and case II (b) showing every 5th trajectory in gray. Trajectories passing the urban area of Leipzig in light purple and mean urban trajectory in purple. The filled areas mark the urban regions of Leipzig (dark grey) and Chemnitz (light grey). Grey boxes denote the rectangular averaging areas used to extract vertical profiles around each trajectory point. The grey arrows indicate the main flow direction of the trajectories.

contain multiple convective cells at different levels of intensity. Within each box, activated number concentrations of cloud droplets and ice crystals, mass mixing ratios of all hydrometeor species, and vertical wind components were averaged across all grid points at each vertical level, generating one vertical profile per experiment every 10 minutes. Layer-thickness-weighted vertical averaging was additionally applied to analyze the temporal evolution of these quantities.

2.3.2 Emission-response analysis

To systematically investigate the relationship between emission strength and cloud microphysical response, we conducted a comprehensive emission-response analysis across all emission experiments. This analysis examines how varying urban emission intensities affect key atmospheric variables and cloud microphysical properties along the trajectories. Using the vertical profiles obtained every 10 minutes along the trajectories for each experiment, we divided the vertical-temporal space into distinct regions to separately analyze different altitude ranges and time periods. For case I, we defined four quadrants (two time periods and two vertical layers), while for case II, the vertical-temporal space was divided into six regions (two time periods and three vertical layers) to account for the more complex vertical structure of this case. Within each region, we performed both vertical and temporal averaging of all microphysical variables. By comparing these region-averaged values across emis-

https://doi.org/10.5194/egusphere-2026-2934
Preprint. Discussion started: 19 June 2026

sion experiments relative to the BASE experiment, we quantified the systematic changes in cloud properties as a function of emission strength. This approach enables systematic assessment of the emission-response relationship and identification of any threshold or non-linear behavior.

3 Results

The two convective precipitation events analyzed in this study developed during the evening hours of 13 and 20 July 2019 near Leipzig, Germany. Both cases are described in detail by Keil et al. (2025), including synoptic conditions and the precipitation and microphysical evolution in the BASE experiment. The two events represent contrasting convective regimes: the first is characterized by a spatially confined convective event which developed under moderate atmospheric instability, while the second features a more extensive and organized convective event which developed under stronger initial instability. This contrast provides a suitable framework for examining how the prevailing meteorological conditions modulates the sensitivity of convective precipitation to urban aerosol loading across a wide range of emission strengths.

3.1 Precipitation sensitivity

3.1.1 Case I

In this case, the convective events formed east of Leipzig, propagated southward, and passed over the city of Chemnitz. The simulated precipitation in the BASE experiment forms a compact, localized system, with a well-defined intense core reaching maximum values of 10 - 12 mm $(4\ \mathrm{h})^{-1}$ (Fig. 3b) downwind of Chemnitz, moving at approximately 4 - 6 m s^{-1}. The core is surrounded by a limited area of moderate precipitation rates (4 - 6 mm $(4\ \mathrm{h})^{-1}$), resulting in a distinct precipitation structure with steep gradients between the intense center and the surrounding regions.

Comparing the emission-scaled scenarios to BASE reveals systematic differences in both precipitation intensity and spatial extent. The experiments NONURBAN, URBANx2, URBANx4, URBANx10, URBANx100 show reduced maximum values around 8 - 10 mm $(4\ \mathrm{h})^{-1}$ (Fig. 3c,d,e,f). In contrast, the high scaled experiments (URBANx500, URBANx1000, URBANx5000) maintain intense cores compared to BASE with maximum values around 10 - 12 mm $(4\ \mathrm{h})^{-1}$. Additionally, the spatial extent of the intense core appears slightly larger and shifts a few kilometers further north than in BASE, indicating not only sustained intensity but also expansion of the most intense precipitation zone and earlier onset of maximum precipitation (Fig. 3g,h,i). Furthermore, in the URBANx1000 and URBANx5000 experiments, a second maximum with 8 - 9 mm $(4\ \mathrm{h})^{-1}$ forms south of the first maximum, indicating that high emission scalings favor the development of multiple convective intensification centers.

The areal coverage of moderate precipitation varies across the experiments relative to BASE. This expansion is particularly evident in the high-scaled experiments, where the moderate precipitation zones extend considerably beyond those in BASE, broadening the system's footprint by several kilometers. The NONURBAN scenario and the lower-to-moderate scaling experiments differ from BASE primarily in the intensity distribution rather than in spatial extent. Overall, these modifications do not

https://doi.org/10.5194/egusphere-2026-2934
Preprint. Discussion started: 19 June 2026

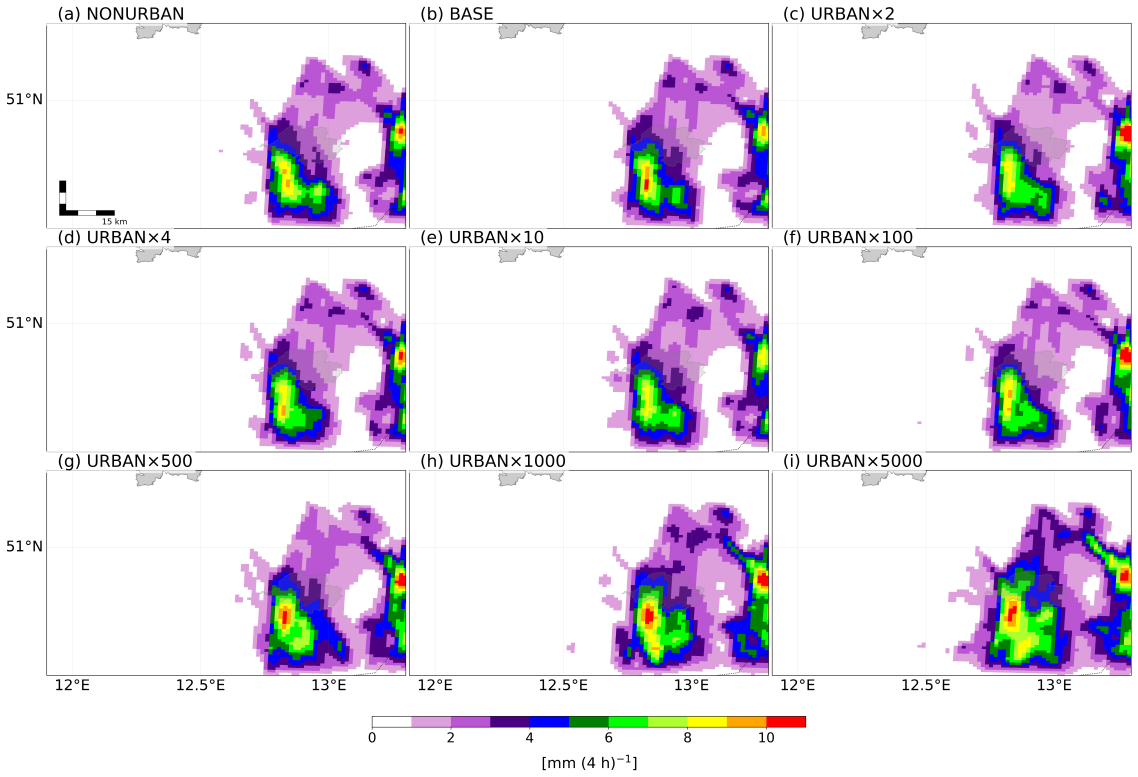

Figure 3. Spatial distribution of accumulated precipitation (19:00 - 23:00 UTC) for case I. Each panel represents a different emission experiment (Tab. 1) with BASE shown in panel (b). Grey and light grey outlines denote city boundaries of Leipzig (upper axis) and Chemnitz, respectively. Note that the boundaries of Chemnitz are hidden by the precipitation field.

scale monotonically with emission strength. The response transitions from weakening (NONURBAN through URBANx100) to intensification and spatial expansion at URBANx500 and above, indicating that qualitatively different behavior emerges only at high emission scalings.

3.1.2 Case II

For case II, the convective event moved diagonal through the upper model domain, starting in the southwest and progressing to the northeastern corner with approximately 15 - 20 m s^{-1}. The accumulated precipitation intensities in the BASE experiment reach values around 20 - 24 mm (4 h)$^{-1}$ (Fig. 4b) after the event passed Leipzig. Within the broader precipitation area, three distinct intensity cores can be identified: a central maximum flanked by northern and southern cores.

Overall precipitation intensities remain remarkably consistent across all scenarios regardless of emission scaling. However, subtle shifts in the internal structure of the precipitation field are evident relative to the BASE case. Across the different experiments, these three cores shift in their spatial positions and vary in their relative intensities. For example, comparing URBANx500 to BASE, the central core appears weaker while the northern and southern cores are intensified (Fig. 4g). The magni-

https://doi.org/10.5194/egusphere-2026-2934
Preprint. Discussion started: 19 June 2026

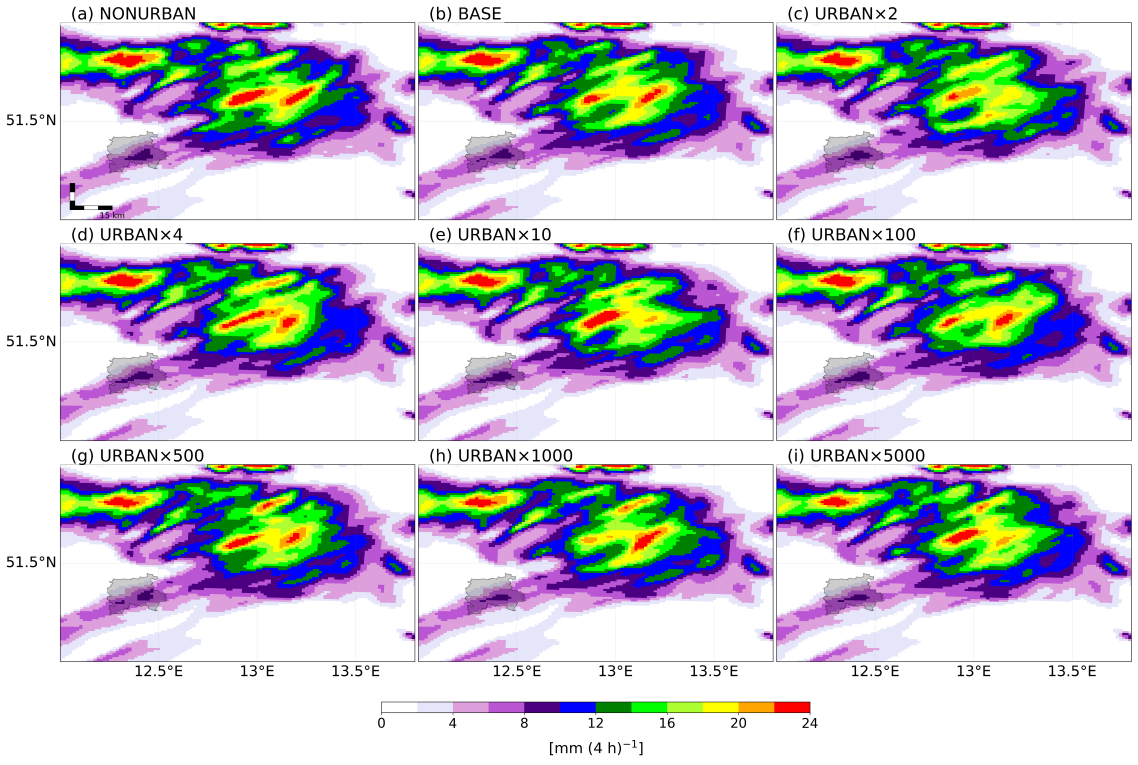

Figure 4. Spatial distribution of accumulated precipitation (17:00 - 21:00 UTC) for case II. Each panel represents a different emission experiment (Tab. 1) with BASE shown in panel (b). Grey outlines denote city boundaries of Leipzig.

tude of these variations remains modest, with differences in local precipitation rates typically on the order of 2 - 4 mm (4 h)$^{-1}$ between scenarios, representing roughly 10 - 20% variability relative to the peak intensities. This indicates that urban emission perturbations produce a detectable but limited shift in the spatial distribution of precipitation. In contrast, the precipitation structure to the northwest, which does not interact with the Leipzig urban area, shows no systematic response across emission scaling factors and remains largely unchanged.

The observed pattern of these shifts does not scale monotonically with emission strength. The spatial configuration and relative intensities of the three cores in URBANx2 and URBANx4 differ from BASE in a manner similar to the higher scalings (URBANx100, URBANx1000, URBANx5000). This response indicates that urban aerosol effects on this convective event remain small across the range of low-to-moderate emission scalings, with the primary impact being a spatial redistribution of precipitation within the multi-cellular structure rather than a substantial modification of total accumulated amounts.

3.2 Microphysics sensitivity

We systematically analyze microphysical evolution by following air volumes along trajectories from Leipzig to the precipitation regions (Fig. 2). This trajectory-based analysis reveals how varying aerosol concentrations modify cloud processes and

https://doi.org/10.5194/egusphere-2026-2934
Preprint. Discussion started: 19 June 2026

Table 2. List of microphysical variables used in this study. Number concentrations (QNI, QNC) are given in cm^{-3}; mixing ratios (QI, QC, QR, QG, QH, QS, Q_{liq}, Q_{ice}) are given in $\mathrm{g\ kg}^{-1}$.

Acronym	Longname
QNI	Number concentration of activated ice crystals
QNC	Number concentration of activated cloud droplets
QI	Cloud ice mixing ratio
QC	Cloud water mixing ratio
QR	Rain water mixing ratio
QG	Graupel mixing ratio
QH	Hail mixing ratio
QS	Snow mixing ratio
Q_{liq}	Liquid hydrometeors (QC + QR)
Q_{ice}	Ice hydrometeors (QI + QG + QH + QS)

influence precipitation development. In case I, trajectories originate approximately 30 km northwest of Leipzig and traverse the city diagonally during 17:50 - 18:40 UTC (Fig. 2a), then advance southeastward for 15 - 20 km before convective lifting elevates them from near-surface to 2 - 4.5 km altitude. The trajectories subsequently undergo southward transport of approximately 80 km within the developing convective event. In case II, trajectories start 40 - 60 km southwest of Leipzig and advance northeastward, crossing the city between 18:00 - 19:00 UTC (Fig. 2b). After passing the city, trajectories move eastward along the urban aerosol plume for approximately 30 minutes before resuming northeastward progression. Convective processes between 20:00 - 21:00 UTC elevate trajectories vertically by 2 - 4.5 km. In both cases, aerosol modifications occur during the Leipzig passage, primarily affecting air volumes before their convective ascent. For detailed temporal and vertical analyses, we focus on representative experiments (BASE, URBANx10, URBANx500, URBANx5000), while the complete emission-response analysis includes all nine emission scalings. The horizontally box averaged approach employed here yields cloud droplet number concentrations below typical in-cloud values, as the analysis volumes encompass both cloudy and predominantly cloud-free regions. Horizontally averaged values reach a maximum of approximately 50 cm^{-3}, compared to in-cloud values ranging from 100 to 600 cm^{-3}, with a mean of around 300 cm^{-3}.

3.2.1 Case I

Temporal microphysical evolution

Figure 5 shows the temporal evolution of horizontally averaged and vertically integrated microphysical properties along trajectories for case I. Activated cloud droplet number concentrations (QNC, Fig. 5a) show varying sensitivity to emission strength. BASE reaches approximately 50 cm^{-3} during both peak periods. URBANx5000 shows consistently reduced val-

https://doi.org/10.5194/egusphere-2026-2934
Preprint. Discussion started: 19 June 2026

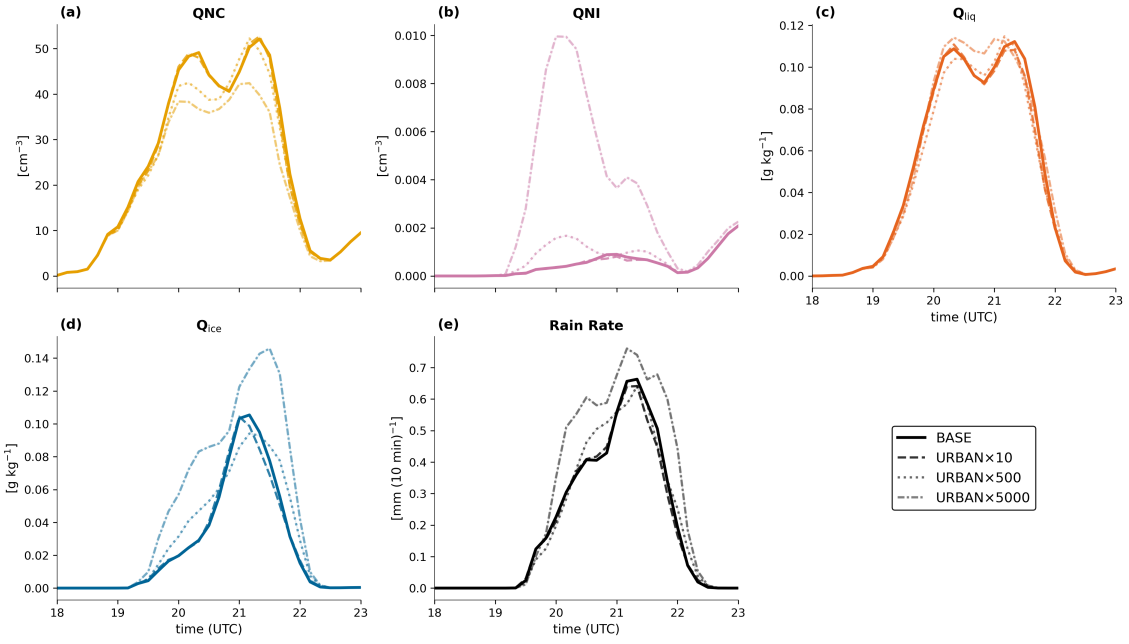

Figure 5. Horizontally averaged and layer-thickness-weighted vertical averages (0 - 13 km) time series for case I of number concentrations of (a) activated cloud droplets (QNC) and (b) activated ice crystals (QNI), as well as mass mixing ratios of (c) Q_{liq}, (d) Q_{ice}; panel(e) shows horizontally averaged rain rates. Line styles correspond to the emission experiments: BASE (solid), URBAN×10 (dashed), URBAN×500 (dotted), URBAN×5000 (dash-dotted).

ues of 35 - 40 cm^{-3} across both peaks, representing a 20 - 30% decrease. URBANx500 exhibits reduction during the first peak (20:15 UTC) but recovers to BASE levels during the second peak (21:30 UTC). This behavior suggests enhanced droplet growth and coalescence at higher aerosol concentrations, with URBANx500 showing intermediate response patterns. In contrast, activated ice crystal concentrations (QNI, Fig. 5b) exhibit the opposite behavior. BASE shows peak values around 0.001 cm^{-3}, while URBANx5000 reaches approximately 0.010 cm^{-3}, corresponding to a tenfold increase. The enhanced ice crystal concentrations suggest that higher aerosol loadings promote ice formation through multiple pathways, including heterogeneous nucleation and immersion freezing of supercooled droplets. URBANx500 displays intermediate values near 0.002 cm^{-3}. URBANx10 remains nearly indistinguishable from BASE for both QNC and QNI, indicating that moderate emission perturbations produce only small effects on particle number concentrations.

Total liquid-phase water content (Q_{liq}, Fig. 5c) shows modest variations between experiments. URBANx5000 exhibits a slightly enhanced first peak, while the second peak occurs earlier than in BASE but maintains a similar magnitude. However, the overall liquid water budget shows only modest changes despite the particle concentration shifts. Detailed analysis reveals compensating trends where cloud water decreases while rain water increases in URBANx5000, resulting in the net increase observed (see supplements Fig. S1). URBANx10 and URBANx500 show minimal deviations from BASE. In contrast, ice-phase hydrometeors (Q_{ice}, Fig. 5d) suggests stronger sensitivity to emission variations.

https://doi.org/10.5194/egusphere-2026-2934
Preprint. Discussion started: 19 June 2026

BASE reaches peak values of 0.105 g kg^{-1}, while URBANx5000 achieves 0.14 g kg^{-1}, approximately 40% higher. The temporal evolution in URBANx5000 reveals earlier enhancement between 19:30 - 20:30 UTC, substantially exceeding BASE throughout this pre-peak period. The subsequent peak forms approximately 30 minutes later than in BASE and exhibits a considerably broader temporal distribution. URBANx500 exhibits intermediate increases with broader temporal spread and delayed peak timing, while URBANx10 shows minimal changes in Q_{ice}. Individual ice species analysis shows that graupel and snow contribute most strongly to the total enhancement, while hail remains below 0.002 g kg^{-1}, despite showing increased processing duration in URBANx5000.

These microphysical modifications translate into measurable precipitation changes. The rain rate (Fig. 5e) increases substantially in the URBANx5000 experiment, reaching peak values of approximately 0.75 mm $(10\ min)^{-1}$ compared to 0.65 mm $(10\ min)^{-1}$ in BASE, representing a 15% increase. URBANx5000 also exhibits elevated rain rates over a broader time period surrounding the peak compared to BASE, indicating sustained intense precipitation beyond the peak itself. This temporal alignment between ice-phase enhancement and precipitation intensification, combined with the tenfold increase in ice crystal concentrations, indicates that ice-phase processes play a key role in precipitation changes for this case.

These results reveal marked differences in sensitivity across the emission scaling range. Moderate perturbations (URBANx10) produce minimal effects across all variables, while high scalings trigger substantial changes primarily in ice-phase processes and precipitation. The responses in URBANx500, showing intermediate behavior between BASE and URBANx5000, further underscore complex non-linear dynamics rather than simple proportional scaling with emission strength.

Vertical-temporal structure

The temporal evolution analysis demonstrates substantial ice-phase enhancement in URBANx5000, but does not reveal the vertical distribution of these changes within the convective system. We therefore examine the vertical-temporal distribution of hydrometeor mass mixing ratios in more detail (Fig. 6). BASE exhibits two distinct maxima for liquid-phase hydrometeors, the first between 19:30 - 20:40 UTC and the second between 20:40 and 22:00 UTC, both reaching approximately 0.6 g kg^{-1}. For the ice-phase hydrometeors (Fig. 6a,e), BASE shows a single concentrated maximum at 3 - 5 km altitude between 20:40 - 21:40 UTC, with peak values around 0.6 g kg^{-1}. URBANx10 produces only modest structural changes, while high scaling factors substantially reorganize the vertical-temporal distribution.

Liquid-phase hydrometeors (Q_{liq}) show complex redistribution patterns under high aerosol loading. URBANx5000 (Fig. 6d) produces enhancements at 1 - 3 km altitude alongside localized reductions, reflecting the compensating QC - QR changes described earlier. This redistribution results from enhanced ice production and strengthened vertical transport modifying the liquid-phase partitioning, with ice formation at higher altitudes subsequently melting to rain while cloud water is converted into ice hydrometeors. URBANx500 (Fig. 6c) shows weaker changes, but a similar pattern as in URBANx5000 before 21:00 UTC.

Ice-phase hydrometeors (Q_{ice}) demonstrate considerably stronger sensitivity to emission variations. URBANx5000 (Fig. 6h) produces substantial increases exceeding 0.4 g kg^{-1} at 3 - 5 km altitude. The temporal distribution extends far beyond the concentrated maximum in BASE, with enhanced ice production persisting over a longer time period. This indicates sustained

https://doi.org/10.5194/egusphere-2026-2934
Preprint. Discussion started: 19 June 2026

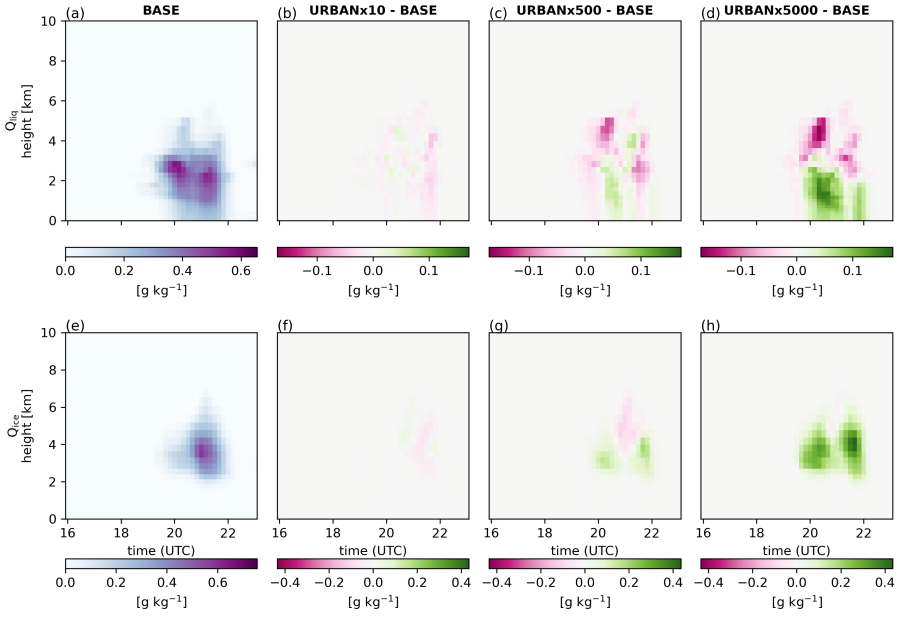

Figure 6. Horizontally averaged vertical-temporal distribution of Q_{liq} (upper row) and Q_{ice} (bottom row) for case I. Panel (a) and (e) show BASE experiment absolute values. Panels (b-d) and (f-h) display differences relative to BASE for URBANx10, URBANx500, and URBANx5000, respectively.

ice-phase convection driven by enhanced ice nucleation and strengthened vertical transport. URBANx500 (Fig. 6g) shows intermediate enhancements up to 0.2 g kg^{-1} with similarly extended temporal distributions.

These vertical structures reveal that strong aerosol perturbations extend the duration of active ice production, substantially modifying the convective structure in this case. The enhancement in peak ice-phase water content reaches approximately 40% in URBANx5000 relative to BASE, demonstrating remarkable intensification of ice-phase processes under high aerosol loading.

These observed ice-phase enhancements suggest potential modifications in vertical motion within the convective system. We therefore examine vertical velocity profiles to assess updraft and downdraft strengths (Fig. 7). BASE (Fig. 7a,e) shows updrafts reaching maximum values around 1.0 m s^{-1} at 2 - 5 km altitude during the time period from 19:00 to 21:00 UTC, with downdrafts of approximately -0.4 m s^{-1}. URBANx10 (Fig. 7b,f) produces minimal changes in vertical velocity structure, consistent with the modest microphysical responses. URBANx5000 shows clear enhancement in both updrafts and downdrafts. URBANx5000 (Fig. 7d,h) exhibits stronger updrafts, increases up to 0.5 m s^{-1} at 2 - 5 km altitude during the time period 19:30 - 21:00 UTC, coinciding temporally with the period of enhanced ice production. The enhanced magnitude relative to BASE align with the enhanced ice-phase observed in the vertical-temporal analysis. Downdrafts are increased up to -0.15 m s^{-1} at 1 - 3 km altitude. URBANx500 (Fig. 7c,g) shows weaker enhancements compared to URBANx5000 but with similar spatial patterns for both up and downdraft.

https://doi.org/10.5194/egusphere-2026-2934
Preprint. Discussion started: 19 June 2026

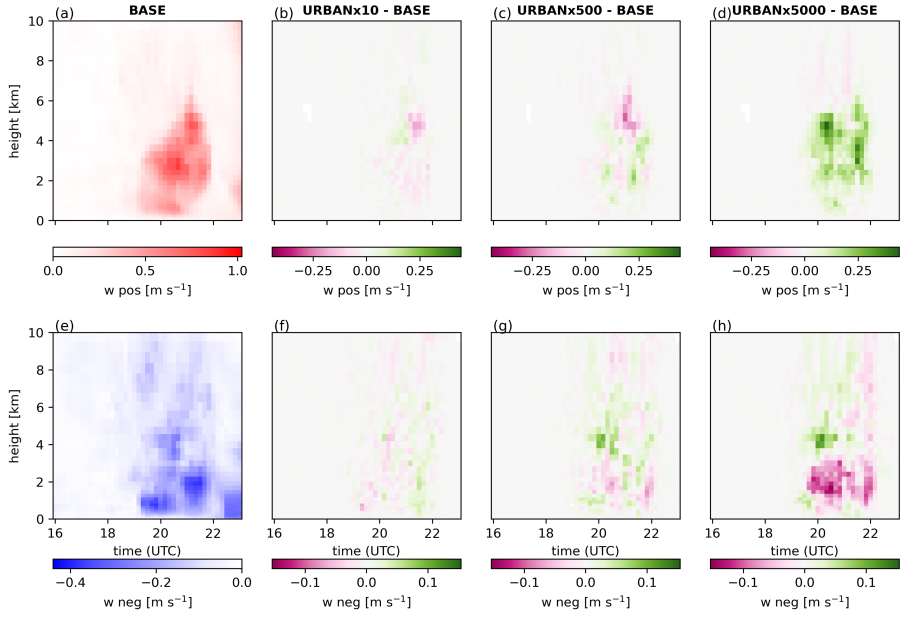

Figure 7. Horizontally averaged vertical-temporal distribution of positive (w pos; upper row) and negative (w neg; lower row) vertical velocities for case I. Panel (a) and (e) show BASE experiment absolute values. Panels (b-d) and (f-h) display differences relative to BASE for URBANx10, URBANx500, and URBANx5000, respectively. Note that the color scale for w neg is reversed, as values are negative.

The strengthened updrafts support enhanced ice nucleation by transporting more liquid water above the freezing level (≈ 2.8 km). This increased ice production releases additional latent heat through freezing, which further intensifies the updrafts, creating a positive feedback loop between microphysical and dynamical processes. The subsequent downdraft enhancement reflects increased precipitation loading from the enhanced ice-phase water content in the aerosol-perturbed cases. These vertical structures demonstrate that high aerosol loading drives a substantial modification of the dynamical and microphysical structure of the convective system.

Emission-response relationships

To systematically quantify the relationship between emission strength and microphysical response, we analyze spatially and temporally averaged values within four quadrants of the vertical-temporal domain (Fig. 8), defined by the selected altitude range and time window. For the early time period (18:00 - 20:40 UTC) at lower altitudes (Fig. 8a), emission scalings up to URBANx100 produce minimal changes. Above URBANx100, liquid-phase hydrometeors exhibit modest increases of approximately 20% for QC and 30% for QR in URBANx5000. QG shows more substantial enhancement, reaching an increase of about 120% in URBANx5000.

At higher altitudes during this period (Fig. 8b), responses become more pronounced. Below URBANx100, differences remain small, but above this threshold, ice-phase hydrometeors increase considerably. In URBANx5000, QNI increases by a

https://doi.org/10.5194/egusphere-2026-2934
Preprint. Discussion started: 19 June 2026

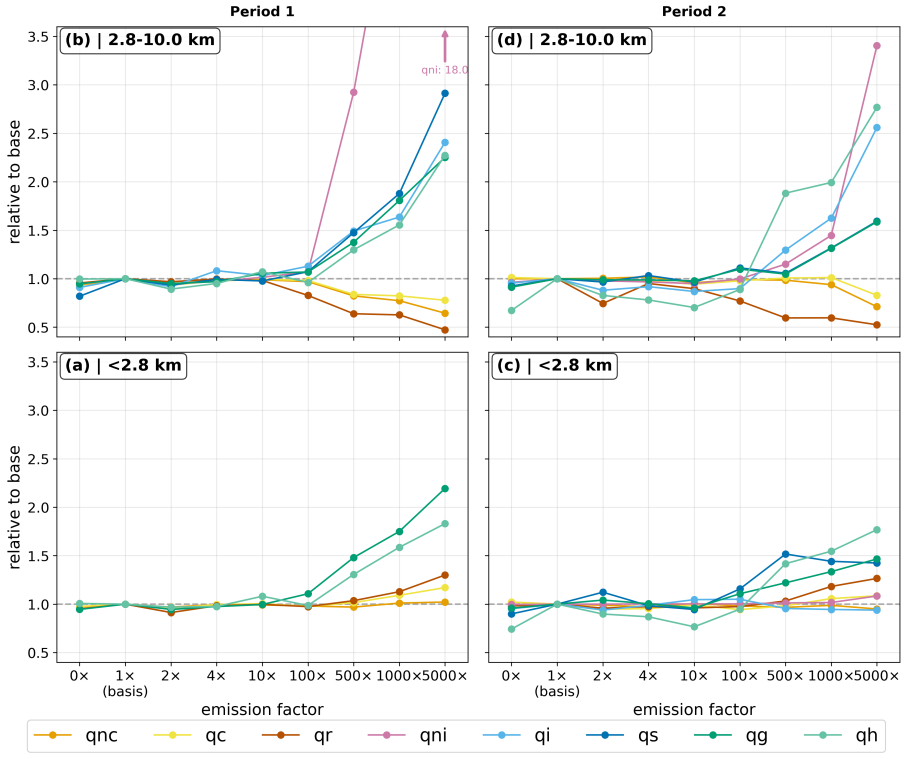

Figure 8. Emission-response relationships for case I showing all microphysical variables as a function of emission scaling factor, displayed as relative change from BASE. Each panel represents one quadrant of the vertical-temporal domain: (a) period 1/ lower altitudes (18:00 - 20:40 UTC, 0 - 2.8 km), (b) period 1/ upper altitudes (20:40 - 23:00 UTC, 2.8 - 10 km), (c) period 2/ lower altitudes (18:00 - 20:40 UTC, 0 - 2.8 km), and (d) period 2/ upper altitudes (20:40 - 23:00 UTC, 2.8 - 10 km).

factor of 18 relative to BASE, QI increases by 140%, QS by 190%, and QG by 125%. Concurrently, liquid-phase hydrometeors decrease markedly in URBANx5000 (QC by 75%, QR by 50%, QNC by 65%), indicating efficient conversion to the ice-phase.

The second time period (20:40 - 23:00 UTC) shows different sensitivities. At lower altitudes (Fig. 8c), QG shows increases beginning at URBANx10, reaching approximately 50% in URBANx5000, while QR and QH exhibit enhanced values in URBANx5000 (+25% and +75%, respectively), with notable changes emerging above URBANx100. At higher altitudes (Fig. 8d), responses are strongest. QNI increases by ≈200% relative to BASE, QI shows increases beginning above URBANx100, reaching 60% in URBANx5000, while QS and QG exhibit approximately 60% enhancement in URBANx5000, with substantial changes above URBANx500. QR shows decreases beginning at URBANx10, reaching 50% reduction in URBANx5000.

These results demonstrate threshold behavior rather than linear scaling with emission strength. Moderate perturbations produce minimal effects across all quadrants, while major changes emerge above a scaling factor of 100 to 500 depending on altitude and time period. The strongest responses occur at higher altitudes, where the inverse relationship between liquid and

https://doi.org/10.5194/egusphere-2026-2934
Preprint. Discussion started: 19 June 2026

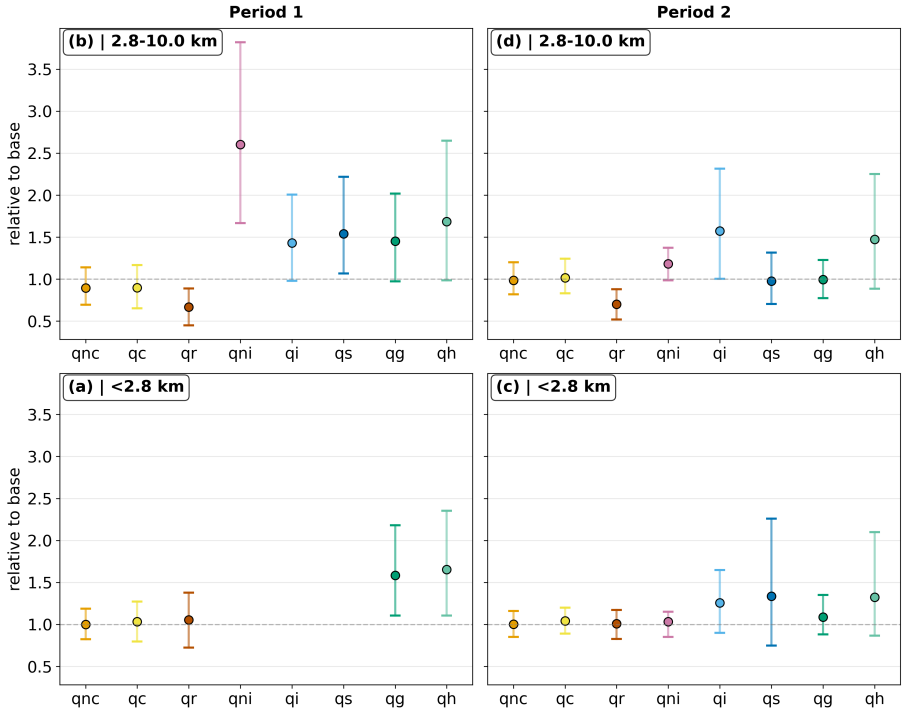

Figure 9. Ensemble variability assessment for case I showing all microphysical variables relative to BASE. Each panel represents one quadrant of the vertical-temporal domain: (a) period 1/ lower altitudes (18:00 - 20:40 UTC, 0 - 2.8 km), (b) period 1/ upper altitudes (20:40 - 23:00 UTC, 2.8 - 10 km), (c) period 2/ lower altitudes (18:00 - 20:40 UTC, 0 - 2.8 km), and (d) period 2/ upper altitudes (20:40 - 23:00 UTC, 2.8 - 10 km). Circles indicate the URBANx500 ensemble mean and error bars represent the minimum to maximum range across ensemble members.

ice-phase species and the strong QNI enhancement reflect efficient ice-dominated microphysical processes consistent with the ice-phase invigoration mechanism documented in the temporal evolution and vertical structure analyses.

Ensemble variability assessment

We examine whether emission-induced changes exceed natural meteorological variability by focusing on URBANx500, which represents a threshold region where substantial microphysical changes start to emerge. Given computational constraints, ensemble simulations were performed for BASE and URBANx500 only. We compare the meteorological ensemble URBANx500 relative to the BASE ensemble (Fig. 9). The meteorological ensemble resembles the range of natural variability arising from slightly different meteorological initial conditions, providing context for evaluating which emission-induced signals are robust against background atmospheric variability.

At uppermost altitudes during the first time period (Fig. 9b), several species show robust emission signals. QNI exhibits the strongest response, with mean values doubling compared to BASE and all ensemble members above baseline. QS is increased

https://doi.org/10.5194/egusphere-2026-2934
Preprint. Discussion started: 19 June 2026

by 60% and QR reduced by approximately 30%, with ranges predominantly above and below baseline respectively. QG, QI, and QH show elevated means with four out of five ensemble members above baseline, indicating a consistent but not fully robust signal. QNC and QC remain close to BASE with substantial variability ranges. During the second time period at higher altitudes (Fig. 9d), QR maintains a robust signal, while QNI and QI show enhancement with four out of five ensemble members above baseline. QS, QG, and QH show increased variability with ranges overlapping BASE. QNC and QC remain close to BASE during both periods. At lower altitudes, QH and QG show enhancement during period 1, while all other variables exhibit ranges overlapping BASE during both periods.

The analysis reveals that while emission effects exist across all scaling factors, their systematic detectability above meteorological variability depends on emission strength and time period. At URBANx500, ice-phase species show particularly robust signals during period 1 at upper altitudes, with QNI, QS, QG, QI, and QH all showing consistent responses across ensemble members. During period 2, QR and QNI and QI maintain robust signals, while other variables show increased variability as the convective event matures. These results indicate that urban aerosol effects on ice-phase microphysics are detectable above natural variability under favorable emission and meteorological conditions, though detectability decreases as the convective event develops.

3.2.2 Case II

Temporal microphysical evolution

Case I demonstrates substantial aerosol sensitivity through ice-phase invigoration under weak synoptic forcing. To assess how meteorological conditions modulate these responses, we examine case II, which features stronger synoptic forcing and a different thermodynamic profile. Figure 10 presents the temporal evolution of horizontally averaged and vertically integrated microphysical properties along trajectories for this contrasting case.

Activated cloud droplet number concentrations (QNC, Fig. 10a) show minimal sensitivity to emission variations. BASE reaches approximately 50 cm^{-3} during maximum cloud development around 20:00 UTC, while URBANx5000 exhibits only modest reduction to 46 cm^{-3}, representing an 8% decrease. URBANx500 and URBANx10 remain nearly indistinguishable from BASE. This weak response contrasts sharply with that of case I, suggesting that droplet growth and coalescence processes are substantially less sensitive to aerosol perturbations under the meteorological conditions of case II. QNI concentrations (Fig. 10b) show BASE values around 0.025 cm^{-3}. URBANx5000 exhibits temporary increases of approximately 0.01 cm^{-3} between 19:00 - 19:30 UTC, but shows reductions afterwards compared to BASE. URBANx500 and URBANx10 show minimal deviations throughout the period.

Total liquid-phase water content (Q_{liq}, Fig. 10c) reaches approximately 0.30 g kg^{-1} at the most developed stage. URBANx5000 and URBANx500 exhibit slight enhancement before the peak is reached but maintain similar maximum values. Detailed analysis reveals modest compensating trends where cloud water (QC) decreases by approximately 0.02 g kg^{-1} in URBANx5000 while rain water (QR) increases correspondingly (see supplements Fig. S2). Ice-phase hydrometeors (Q_{ice}, Fig. 10d) reach peak values of approximately 1.7 g kg^{-1} in BASE. URBANx5000 exhibits only modest increases in maximum

https://doi.org/10.5194/egusphere-2026-2934
Preprint. Discussion started: 19 June 2026

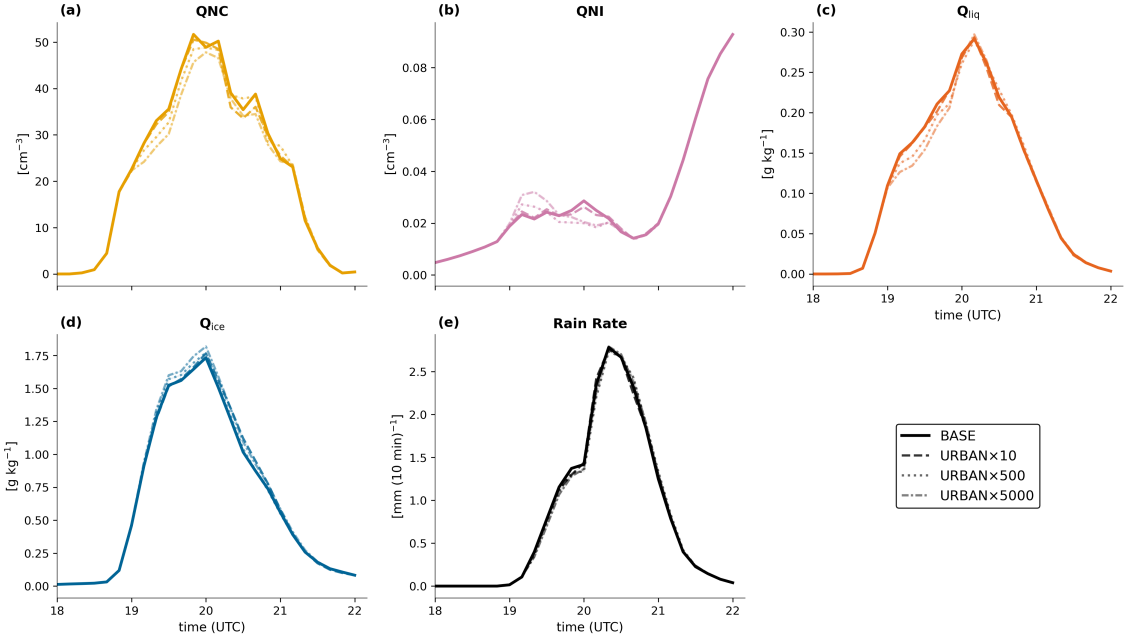

Figure 10. Horizontally averaged and layer-thickness-weighted vertical averages (0 - 13 km) time series for case II of number concentrations of (a) activated cloud droplets (QNC) and (b) activated ice crystals (QNI),as well as mass mixing ratios of (c) Q_{liq} (QC+ QR), (d) Q_{ice} (QI+ QG+ QS+ QH); panel(e) shows horizontally averaged rain rate. Line styles correspond to the emission experiments: BASE (solid), URBAN×10 (dashed), URBAN×500 (dotted), URBAN×5000 (dash-dotted).

values (10% increase), with total ice content is dominated by graupel. Snow (QS) shows the strongest sensitivity with increases of approximately 0.05 g kg^{-1}. URBANx500 and URBANx10 remain close to BASE. Precipitation rates (Fig. 10e) reach maximum values of approximately 2.6 mm (10 min)$^{-1}$ around 20:00 UTC. All emission experiments produce nearly identical rain rates, with only slight reductions in the high emission experiments before 20:00 UTC.

These results demonstrate fundamentally different aerosol sensitivity compared to case I. While URBANx5000 shows moderate cloud water reduction and weak snow enhancement, horizontally averaged ice-phase enhancements (10%) and precipitation changes remain modest compared to the 40% and 15% increases observed in case I. The weaker integrated responses suggest that the meteorological conditions in case II reduce the system's overall susceptibility to aerosol-induced modifications.

Vertical-temporal structure

While the horizontally averaged analysis reveals limited overall responses, examining the vertical-temporal distribution provides insight into whether emission perturbations produce localized structural modifications within the convective event (Fig. 11). The BASE simulation (Fig. 11a,e) exhibits liquid-phase hydrometeors concentrated between 1 - 5 km altitude during 19:00 - 20:30 UTC, reaching peak values of about 0.8 g kg^{-1}. Ice-phase hydrometeors dominate the upper troposphere at 7 - 12 km altitude during the same time period, with maximum values reaching 4 g kg^{-1}.

https://doi.org/10.5194/egusphere-2026-2934
Preprint. Discussion started: 19 June 2026

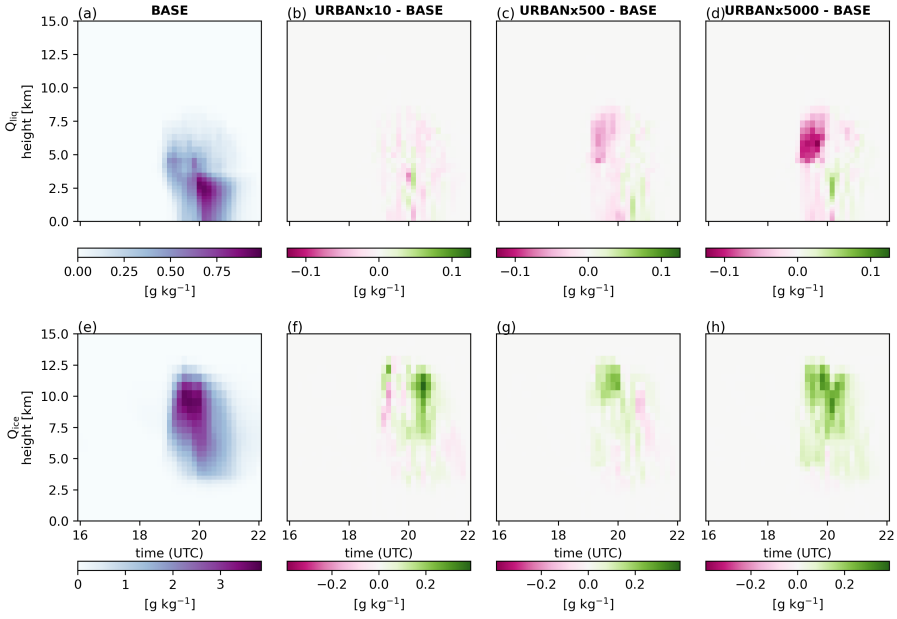

Figure 11. Horizontally averaged vertical-temporal distribution of Q_{liq} (upper row) and Q_{ice} (bottom row) for case II. Panel (a) and (e) show BASE experiment absolute values. Panels (b-d) and (f-h) display differences relative to BASE for URBANx10, URBANx500, and URBANx5000, respectively.

Emission perturbations produce distinct vertical patterns for the liquid and ice-phases. Liquid-phase hydrometeors (Q_{liq}) exhibit negative anomalies that intensify with emission strength. URBANx500 (Fig. 11c) shows reductions at 4 - 8 km altitude before 20:00 UTC, while URBANx5000 (Fig. 11d) produces more pronounced decreases reaching approximately -0.1 g kg^{-1} in the same region. This mid-level liquid water depletion likely reflects enhanced conversion to ice-phase or more efficient precipitation formation processes.

Ice-phase hydrometeors (Q_{ice}) demonstrate systematic enhancements. URBANx10 produces modest positive anomalies after 20:00 UTC, while URBANx500 (Fig. 11g) shows positive anomalies before 20:00 UTC. URBANx5000 (Fig. 11h) exhibits the strongest response, with enhancements reaching 0.4 g kg^{-1} distributed across the 7 - 12 km layer. The vertical extent and timing of these anomalies suggest that emission perturbations enhance ice production at upper levels through strengthened vertical transport of supercooled droplets or enhanced heterogeneous ice nucleation.

The vertical analysis reveals a characteristic pattern in case II, with emission perturbations primarily enhancing upper-level ice-phase content (7 - 12 km) by up to 0.4 g kg^{-1} (10% of BASE peak values) while depleting mid-level liquid water (4 - 8 km) by approximately 0.1 g kg^{-1} (12% of BASE). This vertical decoupling indicates that aerosol effects concentrate where ice formation processes dominate. However, the moderate magnitude of these changes suggests that the overall convective response remains limited despite localized structural modifications.

https://doi.org/10.5194/egusphere-2026-2934
Preprint. Discussion started: 19 June 2026

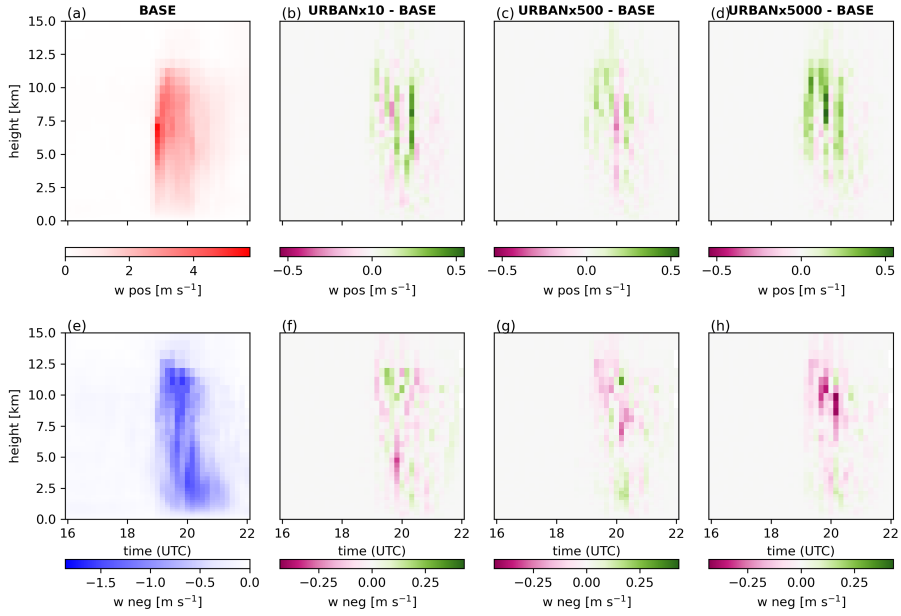

Figure 12. Horizontally averaged vertical-temporal distribution of positive (w pos; upper row) and negative (w neg; lower row) vertical velocities for case II. Panel (a) and (e) show BASE experiment absolute values. Panels (b-d) and (f-h) display differences relative to BASE for URBANx10, URBANx500, and URBANx5000, respectively. Note that the color scale for w neg is reversed, as values are negative.

The upper-level ice-phase enhancements indicate possible changes in vertical velocity structure within the convective event. We therefore evaluate vertical velocity profiles to assess updraft and downdraft strength (Fig. 12). BASE exhibits substantially stronger convective dynamics than case I, with updrafts reaching maximum values around 5 m s^{-1} at 5 - 7.5 km altitude during the period from 19:00 to 19:30 UTC and downdrafts of approximately -1.5 m s^{-1} at 2 - 12 km altitude during 19:30 to 20:30 UTC, reflecting the more extensive and organized nature of this convective event.

Emission perturbations produce spatially variable responses in vertical motion. URBANx10 and URBANx500 show mixed positive and negative anomalies of approximately $\pm$0.5 m s^{-1} for updrafts, without clear systematic patterns. URBANx5000 (Fig. 12d) demonstrates more coherent positive anomalies above 7 km, consistent with the enhanced ice production observed at these upper levels. Downdrafts exhibit enhanced negative anomalies above 7 km around 20:00 UTC in URBANx500 and URBANx5000 (Fig. 12g,h), suggesting strengthened descending motion associated with increased precipitation loading.

Despite the positive updraft anomalies at upper levels in URBANx5000, overall vertical velocity responses remain modest relative to the strong background forcing characterizing this system. Updraft modifications reach approximately 10% indicating that while aerosol perturbations affect upper-level dynamics and ice processes the convective response remains largely controlled by the meteorological environment rather than microphysical interactions.

https://doi.org/10.5194/egusphere-2026-2934
Preprint. Discussion started: 19 June 2026

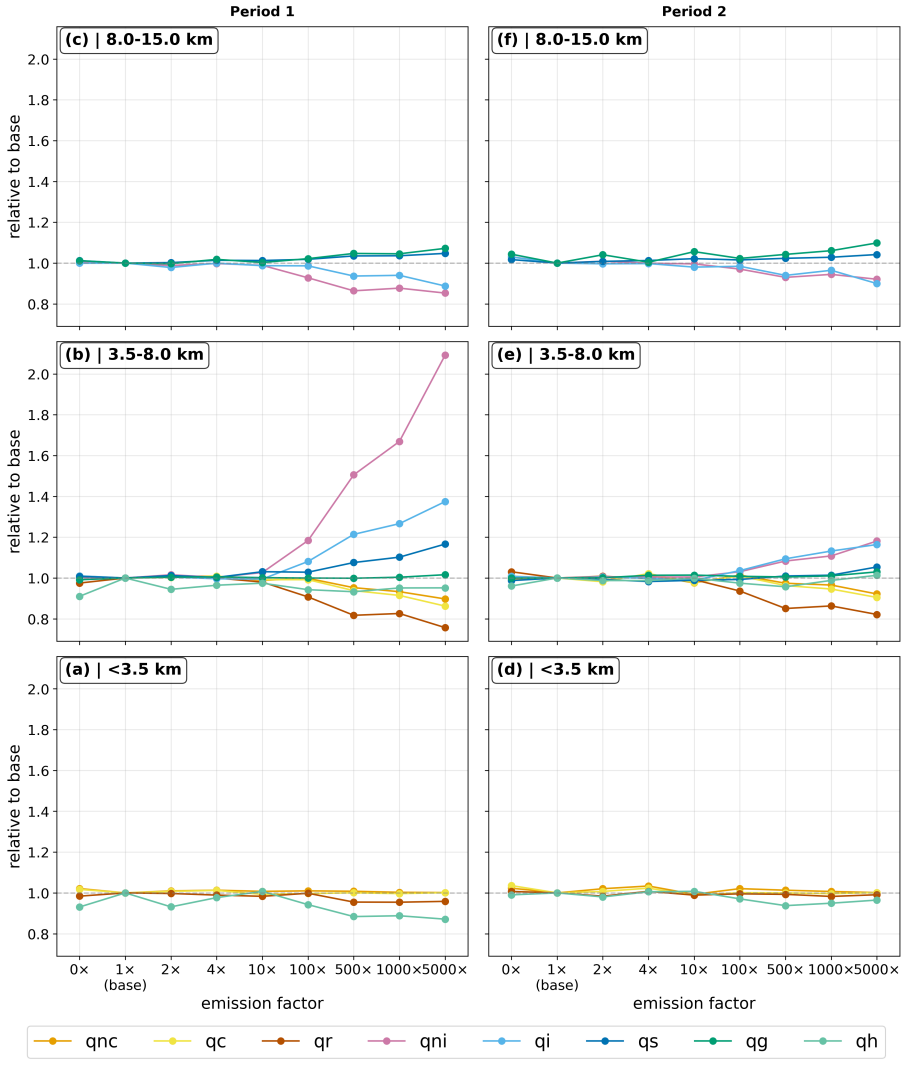

Figure 13. Emission-response relationships for case II showing all microphysical variables as a function of emission scaling factor, displayed as relative change from BASE. Each panel represents one region of the vertical-temporal domain: (a) period 1/lower altitudes (18:00 - 20:00 UTC, 0 - 3.5 km), (b) period 1/mid altitudes (18:00 - 20:00 UTC, 3.5 - 8 km),(c) period 1/upper altitudes (18:00 - 20:00 UTC, 8 - 15 km), (d) period 2/lower altitudes (20:00 - 22:00 UTC, 0 - 3.5 km), (e) period 2/mid altitudes (20:00 - 22:00 UTC, 3.5 - 8 km), and (f) period 2/upper altitudes (20:00 - 22:00 UTC, 8 - 15 km).

Emission-response relationships

To assess the full emission-response relationship, we analyze microphysical properties across all nine emission experiments within six regions of the vertical-temporal domain (Fig. 13). During the first time period (18:00 - 20:00 UTC, Fig. 13a,b,c), the strongest responses occur at mid-level altitudes. Starting with URBANx100, QNI increases by 100 % and QI by 40 % in

https://doi.org/10.5194/egusphere-2026-2934
Preprint. Discussion started: 19 June 2026

URBANx5000, while QS shows 20 % enhancement. Concurrently, QNC and QC decline by 10 - 15 % and QR reduces by 25 %, indicating efficient liquid-to-ice conversion at these altitudes. QG remains largely unchanged, while QH shows slight reductions. At higher altitudes inverse behavior is visible, with QNI and QI decreasing by 10 % while QS and QG increase slightly, suggesting redistribution of ice formation from upper to mid-levels. At lower altitudes minimal changes across all variables appear. During the second time period (20:00 - 22:00 UTC, Fig. 13d,e,f), all responses weaken substantially. Mid-level QNI and QI increase by only 20% in URBANx5000, with QR decreasing by 20 %. Upper altitudes maintain inverse patterns, while lower altitudes remain unresponsive. This temporal weakening likely reflects the maturation of the convective event, where increasingly strong background dynamics progressively dominate over aerosol-induced perturbations.

The emission-response analysis reveals a threshold behavior above URBANx100, but with substantially weaker responses than case I. The strongest sensitivity at mid-levels during the first period, where QNI doubling coincides with 15 - 25 % liquid water reductions, demonstrating active aerosol-microphysics coupling. However, the inverse upper-level responses indicate vertical redistribution rather than net system-wide enhancement. The complex spatial patterns and period-dependent weakening, reflect the buffering effect of stronger meteorological forcing in case II, ultimately limiting the impact of aerosol perturbations on precipitation formation.

Ensemble variability assessment

To assess whether emission-induced changes in case II exceed natural meteorological variability, we compare the URBANx500 meteorological ensemble relative to the BASE ensemble (Fig. 14). At higher altitudes during period 1, QNI shows a robust decrease with four out of five ensemble members below the BASE results. At mid-level altitudes during period 1, QNI shows clear enhancement with all ensemble members above the BASE results, and QI shows consistent increase with four out of five ensemble members above BASE results. All other variables show ranges that overlap or intersect BASE values across both periods and altitude levels, indicating that emission effects at URBANx500 scaling do not emerge robustly above natural atmospheric variability for most species.

The ensemble analysis highlights the dominant influence of meteorological variability versus an aerosol impact. Case I showed robust signals across multiple variables and altitude levels during period 1, while case II exhibits robust signals only for QNI and QI at specific altitude levels, with the opposing response of QNI at upper versus mid-levels reflecting the vertical redistribution pattern identified in the emission-response analysis. Stronger background dynamics in case II substantially reduce the number and magnitude of detectable aerosol-induced modifications.

4 Discussion and conclusion

This study investigates the sensitivity of two convective precipitation events near Leipzig to systematic variations in urban emission strength, using the coupled model system COSMO-DCEP-MUSCAT with direct aerosol-cloud coupling. Both events developed during the evening hours of 13 and 20 July 2019, respectively, and passed through the urban aerosol plume of Leipzig under contrasting convective instability conditions. Urban emission strengths were scaled across nine factors spanning

https://doi.org/10.5194/egusphere-2026-2934
Preprint. Discussion started: 19 June 2026

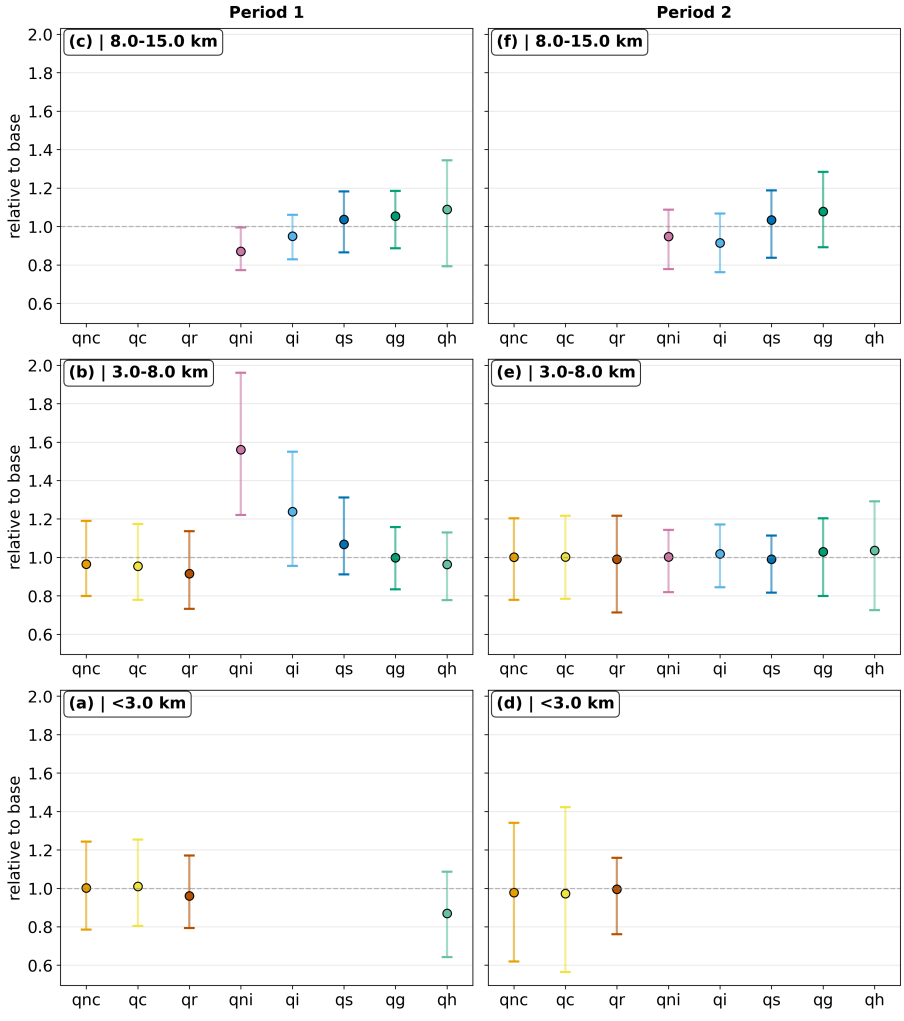

Figure 14. Ensemble variability assessment for case II showing all microphysical variables relative to BASE. Each panel represents one region of the vertical-temporal domain: (a) period 1/lower altitudes (18:00 - 20:00 UTC, 0 - 3.5 km), (b) period 1/mid altitudes (18:00 - 20:00 UTC, 3.5 - 8 km),(c) period 1/upper altitudes (18:00 - 20:00 UTC, 8 - 15 km), (d) period 2/lower altitudes (20:00 - 22:00 UTC, 0 - 3.5 km), (e) period 2/mid altitudes (20:00 - 22:00 UTC, 3.5 - 8 km), and (f) period 2/upper altitudes (20:00 - 22:00 UTC, 8 - 15 km). Circles indicate the URBANx500 ensemble mean and error bars represent the minimum to maximum range across ensemble members.

from zero to 5000 times the current day Leipzig emissions. In order to gain an impression on the sensitivity to slight meteorological variations ensemble simulations were conducted by varying the meteorological spin-up length for the BASE and the URBANx500 experiments. For the distinct evaluation Lagrangian backward trajectory analysis was used to follow the urban air volumes into the convective regions.

https://doi.org/10.5194/egusphere-2026-2934
Preprint. Discussion started: 19 June 2026

The two cases reveal different sensitivities to urban aerosol loading, consistent with previous studies demonstrating that the meteorological conditions modulates aerosol-cloud-precipitation interactions (Khain et al., 2008; Keil et al., 2025). Under moderate convective instability, high emission scalings trigger ice-phase invigoration through enhanced ice nucleation, latent heat release, and strengthened updraft feedback, producing increases in ice content of up to 40% and precipitation intensity of up to 15%, accompanied by spatial expansion of the precipitation field and temporal shifts in maximum precipitation. Under higher convective instability, spatial redistribution of precipitation rather than intensification dominates the response, with even the highest emission scalings producing only modest microphysical modifications, as strong background dynamics limit updraft enhancement and confine aerosol-induced changes to vertical redistribution of hydrometeors rather than system-wide intensification. The stronger background dynamics effectively buffer aerosol-induced impact, a behavior in line with Barthlott and Hoose (2018) and Schneider et al. (2019), who found aerosol sensitivities over central Europe to be substantially reduced under stronger large-scale forcing.

The emission-response analysis reveals non-monotonic behavior and transitions between qualitatively different response regimes that emerge only at high emission scalings, beyond what low-to-moderate perturbations alone would indicate. Among the few studies that have explicitly varied emission or CCN strength, Kawecki et al. (2016) scaled urban emissions from Kansas City by factors of 0.5, 1.0, and 2.0, finding only modest convective responses within this low-to-moderate range. Lucas et al. (2025) and Barthlott and Hoose (2018) prescribed discrete CCN categories ranging from maritime to polluted continental conditions, revealing systematic shifts in microphysical pathways with increasing aerosol loading, yet these approaches prescribe CCN directly rather than modifying emission fields and do not extend beyond observed concentration ranges. The present study extends the scaling range substantially further, enabling the identification of threshold-like transitions and non-monotonic behavior that characterize sensitivity of convective events to urban aerosol loading. This systematic approach reveals response regimes that clean-versus-polluted comparisons or narrow scaling ranges cannot resolve. The extension to high scaling factors provides a first indication of whether the aerosol effect begins to saturate, though a definitive assessment would require additional scaling factors beyond those investigated here.

The ensemble analysis at URBANx500 reveals that robust emission signals are confined to specific variables and time periods, and are more pronounced in case I than in case II. In case I, ice-phase species show the most consistent responses across ensemble members during the first period, while most variables do not emerge clearly above ensemble spread during the second period and at lower altitudes. In case II, stronger background dynamics substantially reduce the number of robustly detectable signals, with opposing responses at different altitude levels reflecting vertical redistribution rather than systematic enhancement. These results indicate that even where a systematic emission-response behavior begins to emerge, the detectability of urban aerosol effects depends strongly on prevailing meteorological conditions, the time period considered, and the variable examined, consistent with the finding of Keil et al. (2025) that ensemble approaches are essential for separating urban aerosol signals from natural meteorological variability.

The methodological approach applied here addresses several recommendations proposed by Varble et al. (2023) and Fan et al. (2025). It includes ensemble simulations to mitigate biases from single-run conclusions, prognostic aerosol representation to allow case-dependent evaluation of mixed-phase convection, and trajectory-based sampling to isolate microphysical

https://doi.org/10.5194/egusphere-2026-2934
Preprint. Discussion started: 19 June 2026

modifications within individual convective clouds from background variability. This provides a more physically consistent basis for attributing aerosol-induced changes to the urban aerosol plume than grid-based analyses that average over large domains.

This study is based on two convective cases only, and while they represent contrasting meteorological situations, the identified emission-response relationships may not generalize to the full range of convective environments typical for mid-latitude urban settings. The emission scaling approach assumes proportional scaling of all emission species, which may not represent realistic emission compositions. In addition, this would effect nonlinear chemical transformations and secondary aerosol formation processes. The CCN and INP activation parameterizations involve assumptions about aerosol size distributions and hygroscopicity that may not fully capture the complexity of real urban aerosol populations. Additionally, the microphysical setup applies saturation adjustment, which may lead to an underestimation of aerosol effects on convective intensity compared to fully explicit supersaturation schemes (Lebo et al., 2012; Zhang et al., 2021), an effect that may be more pronounced at the higher emission scalings examined here.

Despite these limitations, this study provides a systematic characterization of the sensitivity of convective precipitation to urban aerosol loading across a wide range of emission conditions, revealing threshold behaviors and regime-dependent responses that binary comparisons cannot resolve. The contrasting case responses highlight the critical role of the prevailing meteorological situation in determining both the magnitude and detectability of urban aerosol effects on convective precipitation.

Data availability. The COSMO-MUSCAT model output data are archived at German Climate Computing Centre (DKRZ) and are available upon request.

Author contributions. FK performed the COSMO-MUSCAT simulations, conducted the analysis, and prepared the manuscript. BH provided technical support for the simulations and modeling advice. MQ and VM contributed to the project design and scientific discussions. All co-authors reviewed the manuscript and contributed to its design and text.

Competing interests. The authors declare that they have no conflict of interest.

Acknowledgements. The authors thank the COSMO-MUSCAT development team for providing the model code and technical support. The authors are grateful for computing time from the German Climate Computing Center (DKRZ). Recent German-wide emission data were provided on request by the German Environment Agency (Umweltbundesamt, UBA). Building geometries and orography (DGM1) are available from the State Enterprise for Geographic Information and Surveying Saxony (GeoSN; https://www.geodaten.sachsen.de/downloadbereich-digitale-3d-stadtmodelle-4875.html, last access 14 July 2020). The authors thank the DWD for their cooperation and support. Minor grammar and style improvements were made with the assistance of AI tools.

https://doi.org/10.5194/egusphere-2026-2934
Preprint. Discussion started: 19 June 2026

Financial support. This publication was funded by the Deutsche Forschungsgemeinschaft (DFG, German Research Foundation) under Germany's Excellence Strategy – EXC 2037 'CLICCS - Climate, Climatic Change, and Society' – Project Number: 390683824

https://doi.org/10.5194/egusphere-2026-2934
Preprint. Discussion started: 19 June 2026

References

Abdul-Razzak, H. and Ghan, S. J.: A parameterization of aerosol activation: 2. Multiple aerosol types, Journal of Geophysical Research: Atmospheres, 105, 6837–6844, https://doi.org/10.1029/1999JD901161, 2000.

Barthlott, C. and Hoose, C.: Aerosol Effects on Clouds and Precipitation over Central Europe in Different Weather Regimes, Journal of the Atmospheric Sciences, 75, 4247 – 4264, https://doi.org/10.1175/JAS-D-18-0110.1, 2018.

Cotton, W. R. and Walko, R.: Examination of Aerosol-Induced Convective Invigoration Using Idealized Simulations, Journal of the Atmospheric Sciences, 78, 287 – 298, https://doi.org/10.1175/JAS-D-20-0023.1, 2021.

Fagunloye, O. and Diem, J. E.: Observed precipitation enhancement and suppression downwind of a major U.S. city, Urban Climate, 62, 102 562, https://doi.org/10.1016/j.uclim.2025.102562, 2025.

Fan, J., Zhang, Y., Li, Z., Yan, H., Prabhakaran, T., Rosenfeld, D., and Khain, A.: Unveiling Aerosol Impacts on Deep Convective Clouds: Scientific Concept, Modeling, Observational Analysis, and Future Direction, Journal of Geophysical Research: Atmospheres, 130, e2024JD041 931, https://doi.org/https://doi.org/10.1029/2024JD041931, e2024JD041931 2024JD041931, 2025.

Granier, C., Darras, S., Denier van der Gon, H., Doubalova, J., Elguindi, N., Galle, B., Gauss, M., Guevara, M., Jalkanen, J.-P., Kuenen, J., Liousse, C., Quack, B., Simpson, D., and Sindelarova, K.: The Copernicus Atmosphere Monitoring Service global and regional emissions (April 2019 version), Tech. rep., Copernicus Atmosphere Monitoring Service (CAMS), https://doi.org/10.24380/d0bn-kx16, 2019.

Guevara, M., Jorba, O., Tena, C., Denier van der Gon, H., Kuenen, J., Elguindi, N., Darras, S., Granier, C., and Pérez García-Pando, C.: Copernicus Atmosphere Monitoring Service TEMPOral profiles (CAMS-TEMPO): global and European emission temporal profile maps for atmospheric chemistry modelling, Earth System Science Data, 13, 367–404, https://doi.org/10.5194/essd-13-367-2021, 2021.

Han, J.-Y., Baik, J.-J., and Khain, A. P.: A numerical study of urban aerosol impacts on clouds and precipitation, Journal of the atmospheric sciences, 69, 504–520, https://doi.org/10.1175/JAS-D-11-071.1, 2012.

Heinold, B., Weger, M., Knoth, O., Schrödner, R., Müller, T., and Tõnisson, L.: High-Resolution Air-Quality Modeling in Urban Areas-A Case Study for the City of Leipzig, in: Air Pollution Modeling and Its Application XXVII, edited by Mensink, C., Gong, W., and Hakami, A., pp. 2–3, Springer International Publishing, Cham, Switzerland, proceedings of the 37th International Technical Meeting on Air Pollution Modelling and Its Application, Hamburg, Germany, 23-27 September 2019, 2019.

Hersbach, H., Bell, B., Berrisford, P., Hirahara, S., Horányi, A., Muñoz-Sabater, J., Nicolas, J., Peubey, C., Radu, R., Schepers, D., et al.: The ERA5 global reanalysis, Quarterly Journal of the Royal Meteorological Society, 146, 1999–2049, https://doi.org/10.1002/qj.3803, 2020.

Inness, A., Ades, M., Agustí-Panareda, A., Barré, J., Benedictow, A., Blechschmidt, A.-M., Dominguez, J. J., Engelen, R., Eskes, H., Flemming, J., Huijnen, V., Jones, L., Kipling, Z., Massart, S., Parrington, M., Peuch, V.-H., Razinger, M., Remy, S., Schulz, M., and Suttie, M.: The CAMS reanalysis of atmospheric composition, Atmospheric Chemistry and Physics, 19, 3515–3556, https://doi.org/10.5194/acp-19-3515-2019, 2019.

Kawecki, S., Henebry, G. M., and Steiner, A. L.: Effects of urban plume aerosols on a mesoscale convective system, Journal of the Atmospheric Sciences, 73, 4641–4660, https://doi.org/10.1175/JAS-D-16-0084.1, 2016.

Keil, F., Quante, M., Heinold, B., and Matthias, V.: Tracking the Impact of Urban Air Masses on Convective Precipitation: A Multi-Member Modeling Study, EGUsphere, 2025, 1–27, https://doi.org/10.5194/egusphere-2025-4374, 2025.

Khain, A. P., BenMoshe, N., and Pokrovsky, A.: Factors Determining the Impact of Aerosols on Surface Precipitation from Clouds: An Attempt at Classification, Journal of the Atmospheric Sciences, 65, 1721 – 1748, https://doi.org/10.1175/2007JAS2515.1, 2008.

https://doi.org/10.5194/egusphere-2026-2934
Preprint. Discussion started: 19 June 2026

Lebo, Z. J., Morrison, H., and Seinfeld, J. H.: Are simulated aerosol-induced effects on deep convective clouds strongly dependent on saturation adjustment?, Atmospheric Chemistry and Physics, 12, 9941–9964, https://doi.org/10.5194/acp-12-9941-2012, 2012.

Lucas, L., Barthlott, C., Hoose, C., and Knippertz, P.: Aerosol effects on convective storms under pseudo-global warming conditions: insights from case studies in Germany, Atmospheric Chemistry and Physics, 25, 18 527–18 548, https://doi.org/10.5194/acp-25-18527-2025, 2025.

Martilli, A., Clappier, A., and Rotach, M. W.: An urban surface exchange parameterisation for mesoscale models, Boundary-layer meteorology, 104, 261–304, https://doi.org/10.1023/A:1016099921195, 2002.

Pruppacher, H. R. and Klett, J. D.: Microphysics of Clouds and Precipitation, Atmospheric and Oceanographic Sciences Library, Springer, 2nd ed. edn., https://doi.org/10.1007/978-0-306-48100-0, 1997.

Rosenfeld, D., Lohmann, U., Raga, G. B., O'Dowd, C. D., Kulmala, M., Fuzzi, S., Reissell, A., and Andreae, M. O.: Flood or drought: How do aerosols affect precipitation?, science, 321, 1309–1313, https://doi.org/10.1126/science.1160606, 2008.

Sarangi, C., Tripathi, S., Qian, Y., Kumar, S., and Ruby Leung, L.: Aerosol and urban land use effect on rainfall around cities in Indo-Gangetic Basin from observations and cloud resolving model simulations, Journal of Geophysical Research: Atmospheres, 123, 3645–3667, https://doi.org/10.1002/2017JD028004, 2018.

Schättler, U., Doms, G., and Schraff, C.: A description of the nonhydrostatic regional COSMO-model. Part VII: User's guide, Deutscher Wetterdienst, https://doi.org/10.5676/DWD_pub/nwv/cosmo-doc_5.05_VII, 2018.

Schneider, C., Pelzer, M., Tönges-Schuller, N., Nacken, M., and Niederau, A.: ArcGIS basierte Lösung zur detaillierten, deutschlandweiten Verteilung (Gridding) nationaler Emissionsjahreswerte auf Basis des Inventars zur Emissionsberichterstattung, Umweltbundesamt UBA-FB-002360, Texte 71/2016, ISSN 1862–4804, 2016.

Schneider, L., Barthlott, C., Hoose, C., and Barrett, A. I.: Relative impact of aerosol, soil moisture, and orography perturbations on deep convection, Atmospheric Chemistry and Physics, 19, 12 343–12 359, https://doi.org/10.5194/acp-19-12343-2019, 2019.

Schubert, S., Grossman-Clarke, S., and Martilli, A.: A double-canyon radiation scheme for multi-layer urban canopy models, Boundary-layer meteorology, 145, 439–468, https://doi.org/10.1007/s10546-012-9728-3, 2012.

Seifert, A. and Beheng, K.: A two-moment cloud microphysics parameterization for mixed-phase clouds. Part 2: Maritime vs. continental deep convective storms, Meteorology and Atmospheric Physics, 92, 67–82, https://doi.org/10.1007/s00703-005-0113-3, 2006a.

Seifert, A. and Beheng, K. D.: A two-moment cloud microphysics parameterization for mixed-phase clouds. Part 1: Model description, Meteorology and atmospheric physics, 92, 45–66, https://doi.org/10.1007/s00703-005-0112-4, 2006b.

Souri, A. H., Choi, Y., Kodros, J. K., Jung, J., Shpund, J., Pierce, J. R., Lynn, B. H., Khain, A., and Chance, K.: Response of Hurricane Harvey's rainfall to anthropogenic aerosols: A sensitivity study based on spectral bin microphysics with simulated aerosols, Atmospheric Research, 242, 104 965, https://doi.org/10.1016/j.atmosres.2020.104965, 2020.

Sprenger, M. and Wernli, H.: The LAGRANTO Lagrangian analysis tool – version 2.0, Geoscientific Model Development, 8, 2569–2586, https://doi.org/10.5194/gmd-8-2569-2015, 2015.

Van Den Heever, S. C. and Cotton, W. R.: Urban aerosol impacts on downwind convective storms, Journal of Applied Meteorology and Climatology, 46, 828–850, https://doi.org/10.1175/JAM2492.1, 2007.

Varble, A. C., Igel, A. L., Morrison, H., Grabowski, W. W., and Lebo, Z. J.: Opinion: A critical evaluation of the evidence for aerosol invigoration of deep convection, Atmospheric Chemistry and Physics, 23, 13 791–13 808, https://doi.org/10.5194/acp-23-13791-2023, 2023.

Weger, M., Heinold, B., Engler, C., Schumann, U., Seifert, A., Fößig, R., Voigt, C., Baars, H., Blahak, U., Borrmann, S., Hoose, C., Kaufmann, S., Krämer, M., Seifert, P., Senf, F., Schneider, J., and Tegen, I.: The impact of mineral dust on cloud formation during the Saharan

https://doi.org/10.5194/egusphere-2026-2934
Preprint. Discussion started: 19 June 2026

dust event in April 2014 over Europe, Atmospheric Chemistry and Physics, 18, 17 545–17 572, https://doi.org/10.5194/acp-18-17545-2018, 2018.

Wolke, R., Knoth, O., Hellmuth, O., Schröder, W., and Renner, E.: The parallel model system LM-MUSCAT for chemistry-transport simulations: Coupling scheme, parallelization and applications, in: Parallel Computing, edited by Joubert, G., Nagel, W., Peters, F., and Walter, W., vol. 13 of *Advances in Parallel Computing*, pp. 363–369, North-Holland, https://doi.org/10.1016/S0927-5452(04)80048-0, 2004.

Wolke, R., Schröder, W., Schrödner, R., and Renner, E.: Influence of grid resolution and meteorological forcing on simulated European air quality: A sensitivity study with the modeling system COSMO–MUSCAT, Atmospheric Environment, 53, 110–130, https://doi.org/10.1016/j.atmosenv.2012.02.085, aQMEII: An International Initiative for the Evaluation of Regional-Scale Air Quality Models - Phase 1, 2012.

Xiao, H., Yin, Y., Chen, Q., and Zhao, P.: Impact of aerosol and freezing level on orographic clouds: A sensitivity study, Atmospheric Research, 176-177, 19–28, https://doi.org/10.1016/j.atmosres.2016.02.014, 2016.

Zhang, Y., Fan, J., Li, Z., and Rosenfeld, D.: Impacts of cloud microphysics parameterizations on simulated aerosol–cloud interactions for deep convective clouds over Houston, Atmospheric Chemistry and Physics, 21, 2363–2381, https://doi.org/10.5194/acp-21-2363-2021, 2021.

Zheng, Z., Zhao, C., Lolli, S., Wang, X., Wang, Y., Ma, X., Li, Q., and Yang, Y.: Diurnal variation of summer precipitation modulated by air pollution: observational evidences in the Beijing metropolitan area, Environmental Research Letters, https://doi.org/10.1088/1748-9326/ab99fc, 2020.

Zhong, S., Qian, Y., Zhao, C., Leung, R., Wang, H., Yang, B., Fan, J., Yan, H., Yang, X.-Q., and Liu, D.: Urbanization-induced urban heat island and aerosol effects on climate extremes in the Yangtze River Delta region of China, Atmospheric Chemistry and Physics, 17, 5439–5457, https://doi.org/10.5194/acp-17-5439-2017, 2017.